Chemistry Europe
European Chemical Societies Publishing

Subphthalocyanine-Diketopyrrolopyrrole Conjugates: 3D Star-Shaped Systems as Non-Fullerene Acceptors in Polymer Solar Cells with High Open-Circuit Voltage

Maria J. Álvaro-Martins,[a] José G. Sánchez,[b] Giulia Lavarda,[c] Desiré Molina,[a] Josep Pallarès,[b] Tomás Torres,*[c, d, e] Lluis F. Marsal,*[b] and Ángela Sastre-Santos*[a]

Dedicated to Prof. Dr. Nazario Martín on the occasion of his 65th birthday

Four star-shaped electron acceptors (C_1-OPh, C_3-OPh, C_1-Cl and C_3-Cl) based on a subphthalocyanine core bearing three diketopyrrolopyrrole wings linked by an acetylene bridge have been synthesized. These derivatives feature two different axial substituents (*i.e.*, 4-*tert*-butylphenoxy (OPh) or chlorine (Cl)) and for each of them, both the C_1 and the C_3 regioisomers have been investigated. The four compounds exhibit a broad absorption band in the 450–700 nm region, with bandgap values near to 2 eV. These materials were applied in the active layer of inverted bulk-heterojunction polymer solar cells in combination with the donor polymer PBDB-T. Derivatives bearing the OPh axial group showed the best performances, with C_1-OPh being the most promising with a PCE of 3.27 % and a V_{oc} as high as 1.17 V. Despite presenting the widest absorption range, the photovoltaic results obtained with C_1-Cl turned out to be the lowest (PCE = 1.01 %).

Introduction

Bulk-heterojunction (BHJ) polymer solar cells have shown great potential for the fabrication of lightweight, flexible and transparent devices with low-cost manufacturing.[1] In conventional BHJ-polymer solar cells, indium tin oxide (ITO) is used as the anode, whereas poly(3,4-ethylenedioxy-thiophene):poly (styrenesulfonate) (PEDOT:PSS) and calcium are used as the hole-transporting layer (HTL) and the electron-transporting layer (ETL), respectively.[2] On the other hand, in BHJ-polymer solar cells with inverted structure, ITO acts as the cathode, calcium is replaced by titanium oxide (TiO_2),[3] zinc oxide (ZnO)[4] or poly[(9,9-bis(3-(*N,N*-dimethylamino) propyl)-2,7-fluorene)-alt-2,7-(9,9 dioctylfluorene)] (PFN)[5] as ETL, meanwhile PEDOT:PSS is replaced by vanadium oxide (V_2O_5)[6] or molybdenum oxide (MoO_3)[7] as HTL. In the last years, electron-accepting fullerenes such as [6,6]-phenyl-C_{70}-butyric acid methyl ester ($PC_{70}BM$) or bis (1-[3-(methoxycarbonyl)propyl]-1-phenyl)-[6,6]C_{62} (Bis-PCBM) have led the polymer solar cells field since they allow for the preparation of highly efficient devices.[8] Nonetheless, the weak absorption in the visible region and poor ambient stability of fullerene materials limit the performance and lifetime of polymer solar cells. Moreover, the high electron affinity of fullerenes limits the open-circuit voltage to values below 1 volt.[9] To overcome these disadvantages, several non-fullerene acceptors (NFA) materials are being developed, which are attracting much attention by virtue of their low energy loss, strong absorption in the visible range, good thermal stability, and lower-cost synthesis with respect to fullerene acceptors.[10] A successful approach for the preparation of NFA materials consists in the synthesis of trimeric and tetrameric species to mimic the spherical shape of the fullerene π-system,[11] which is assumed to be capable of aligning with the donor π-plane in a three-dimensional (3D) way decreasing the Coulomb barrier for charge separation due to enhanced entropic effects, thus enabling isotropic charge transport compared to one-dimensional.[12]

Due to their unusual characteristics, subphthalocyanines (SubPcs) and diketopyrrolopyrroles (DPPs) stand out among other chromophores for the preparation of NFA materials.[13] SubPcs are aromatic chromophores with 14 delocalized π-electrons and a boron atom at their central cavity. These derivatives have been widely investigated in organic solar cells (OSCs) because of their interesting optical and electronic properties, such as strong optical absorptions in the 460–580 nm spectral region, and relatively high electron mobilities.

[a] *M. J. Álvaro-Martins, Dr. D. Molina, Prof. Á. Sastre-Santos*
Instituto de Bioingeniería
Universidad Miguel Hernández
03202 Elche (Spain)
E-mail: asastre@umh.es
[b] *Dr. J. G. Sánchez, Dr. J. Pallarès, Prof. L. F. Marsal*
Departament d'Enginyeria Electronica Electrica i Automatica
Universitat Rovira i Virgili
43007 Tarragona (Spain)
E-mail: lluis.marsal@urv.cat
[c] *G. Lavarda, Prof. T. Torres*
Departamento de Química Orgánica,
Universidad Autónoma de Madrid (Spain)
E-mail: tomas.torres@uam.es
[d] *Prof. T. Torres*
IMDEA-Nanociencia
Campus de Cantoblanco, 28049 Madrid (Spain)
[e] *Prof. T. Torres*
Institute for Advanced Research in Chemical Sciences (IAdChem)
Universidad Autónoma de Madrid (Spain)

Supporting information for this article is available on the WWW under https://doi.org/10.1002/cplu.202100103

Besides, their cone-shaped structure prevents aggregation in solution and even in the solid state.[14] Traditionally, they have been applied as electron donors in BHJ organic solar cells,[15] although it has been shown that they can also act as electron acceptors in solution-processed BHJ devices.[11a,b,16] Thus, a 8.4% PCE record is held by Cnops when they fabricated three-layer vacuum-deposited devices, combining SubPc and SubNc in a two-step exciton dissociation process[17] Regarding solution-processed devices, SubPc-cores funcionalized with three imide groups resulted in a maximum efficiency of 4.92%, using the polymer PM6 as donor counterpart.[18]

On the other hand, DPPs are well-known building blocks characterized by great synthetic versatility, high physical and chemical stability, and outstanding optoelectronic properties, such as intense radiation absorption in the visible spectrum and high fluorescence quantum yields.[19] The usual chemical structure of these moieties includes a central electron-attracting bicyclic-dilactam core flanked by two aromatic rings (*e.g.* benzene, thiophene, furan, selenophene, etc.). The flat structure of the DPP-core leads to significant π-π interactions and the dihedral angle that these rings form concerning the core influences the final morphology of the systems where they are integrated. On the grounds of these characteristics, these moieties have also been extensively investigated in BHJ OSCs, as both donor and acceptor systems.[20]

Herein, we have designed and synthesized four new NFAs that combine SubPcs and DPPs into 3D star-shaped structures (Scheme 1). The four acceptors present two main structural differences. First, two of them feature a *tert*-butylphenoxy group (OPh) in the axial position of the SubPc macrocycle (*i.e.* ***C*$_1$-OPh 1** and ***C*$_3$-OPh 2**), whereas the other two bear a chlorine (Cl) atoms in the same position (*i.e.* ***C*$_1$-Cl 3** and ***C*$_3$-Cl 4**). Besides, for each axial ligand, both the C_1- and the C_3-symmetric regioisomers have been prepared. The solid-state morphology within the donor-acceptor blend and the optoelectronic properties of the materials are strongly influenced by these structural features (*vide infra*), which ultimately affect the photovoltaic performances of the devices based on these derivatives. With the aim to elucidate which structural features of the NFAs are the most favourable for their application in BHJ OSCs, we studied these acceptor systems blended with the electron-donating polymer poly[(2,6-(4,8-bis(5-(2-ethylhexyl)thiophen-2-yl)-benzo[1,2-b:4,5-b']dithiophene))alt-(5,5-(1',3'-di-2-thienyl-5',7'-bis(2-ethylhexyl)benzo[1',2'c:4',5'-c'] dithiophene-4,8-dione)] (PBDB-T) in BHJ-inverted polymer solar cells. PBDB-T was chosen as donor material due to its complementary absorption band and deep HOMO level, which allow to obtain higher circuit current density (J_{SC}) and V_{OC}, respectively, in devices fabricated with subphthalocyanine acceptors. The BHJ-inverted polymer solar cells were fabricated using ITO as the cathode, TiO_2 as the ETL, V_2O_5 as the HTL, and silver (Ag) as the anode (ITO/TiO_2/PBDB-T:-SubPc(DPP)$_3$/V_2O_5/Ag). The effects of the 1,8-diiodooctane (DIO) additive concentration and annealing temperature on the performance of the devices were also analysed. Remarkably, compound ***C*$_1$-Cl 3** showed the lowest parameters, despite its wide absorbance range. On the other hand, ***C*$_1$-OPh 1** turned out to be the best the candidate among the series for application as NFA in BHJ solar cells. The J_{SC} trend calculated from the current density-voltage (*J*) curves is corroborated by the integrated J_{SC} calculated from the external quantum efficiency (EQE) spectrum for all devices.

Results and Discussion

The chemical structures of the four derivatives were confirmed by ^{1}H NMR, ^{11}B NMR and FT-IR spectroscopies as well as by MALDI-TOF mass spectrometry (see the Supporting Information, Figure S1–16). The ^{1}H NMR spectra of the C_1-symmetric derivatives, *i.e.* ***C*$_1$-OPh 1** and ***C*$_1$-Cl 3**, have a similar profile. The same applies for C_3-symmetric derivatives ***C*$_3$-OPh 2** and ***C*$_3$-Cl 4**. A slightly shift towards lower fields of the protons around 8.0 ppm and 8.8–8.9 ppm corresponding to the SubPc ring was observed comparing the SubPc-Cl **3** and **4** with their analogues with the phenoxy group in the axial position **1** and **2** (Figure S15). Spectra of ***C*$_1$-OPh 1** and ***C*$_3$-OPh 2** show slight differences in the aromatic region, namely for the signals between 8.84–8.80 ppm belonging to the DPP units, which appear for ***C*$_1$-OPh 1** in the form of two overlapping doublets centered at 8.83 ppm and 8.82 ppm and for ***C*$_3$-OPh 2** as two doublet of doublets centered at 8.81 ppm (Figure S13). Such unresolved signals in the spectrum of ***C*$_1$-OPh 1** are indicative of a rupture of the symmetry environment, which give rise to a

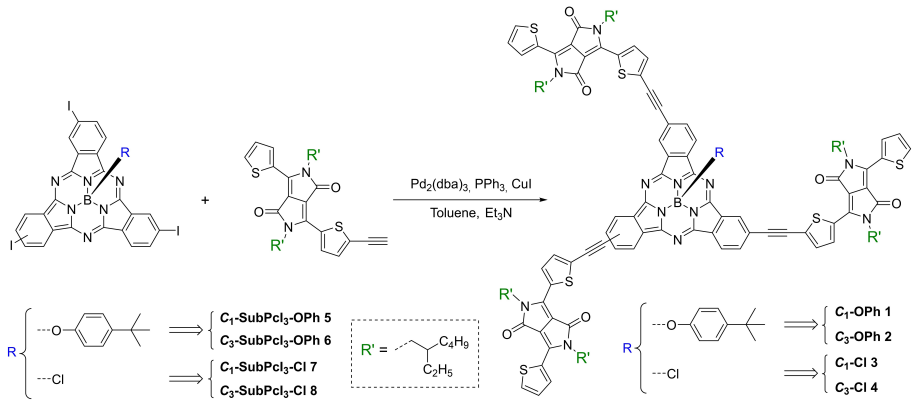

Scheme 1. Synthetic scheme for the preparation of SubPc-(DPP)$_3$ derivatives **1**–**4**.

more complex pattern.[21] In the case of the ***C*$_1$-Cl 3** and ***C*$_3$-Cl 4** spectra, the same behaviour was observed (Figure S14). Regarding to ^{11}B NMR spectra, a single singlet signal was observed in all spectra appearing at −14.60 ppm for OPh derivatives and −12.9 and −13.9 ppm for ***C*$_1$-Cl 3** and ***C*$_1$-Cl 4**, respectively.

Optical and electronic properties

The absorption features of all these SubPc-DPP derivatives measured in $CHCl_3$ solutions are shown in Figure 1a-1d and Table 1. All the acceptor materials show absorption bands in the ultraviolet (250–450 nm) and the visible/near IR (450–700 nm) regions of the spectra, Figure 1a-1b. The spectra of ***C*$_1$-OPh 1**, ***C*$_3$-OPh 2** and ***C*$_3$-Cl 4** present the characteristic shape typically observed for SubPc chromophores, showing maxima at 654, 623, 624 nm, respectively. Besides, all three spectra exhibit a shoulder attributable to the DPP units at 553, 550, and 554 nm, respectively. Differently, the UV-vis spectrum of ***C*$_1$-Cl 3** shows a broader Q-band at 592 nm with a molar extinction coefficient lower than the other derivatives (Figure 1d, Table 1). We infer that the existence of orbital overlap between the chromophoric units in ***C*$_1$-Cl 3** could lead to a strong interaction in the ground state. In comparison with the corresponding reference compounds (**DPP Ref.**, **SubPc 5**, **6**, **7** and **8**) the four acceptors suffers a red-shift of the Q-band. ***C*$_3$-OPh 2** suffers the

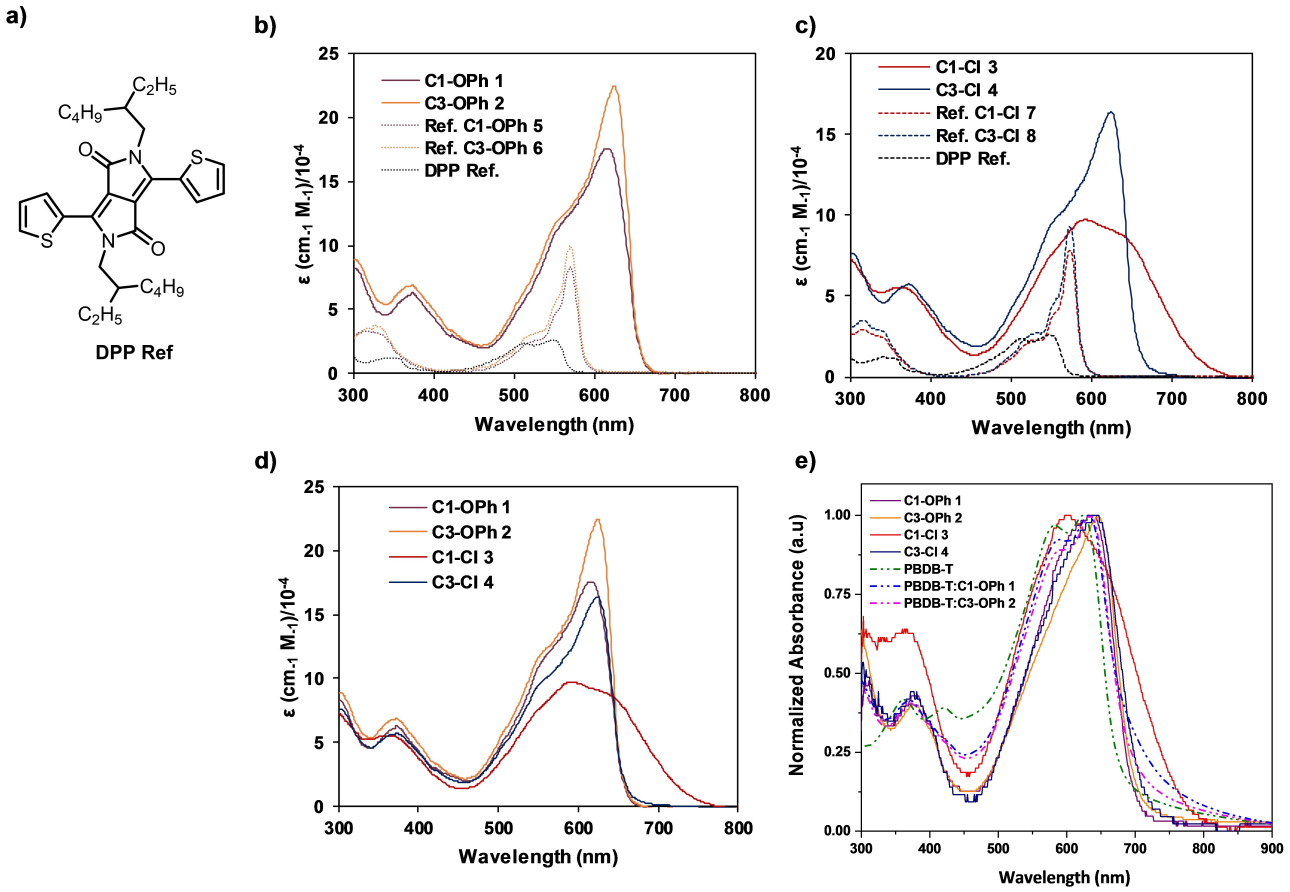

Figure 1. a) Chemical structure of DPP Ref. Absorption spectra of: b) ***C*$_1$-OPh 1**, ***C*$_3$-OPh 2** (solid lines) and the corresponding precursors ***C*$_1$-SubPcl$_3$-OPh 5** and ***C*$_3$-SubPcl$_3$-OPh 6** (dashed lines) in $CHCl_3$. c) ***C*$_1$-Cl 3**, ***C*$_3$-Cl 4** (solid lines) and the corresponding precursors ***C*$_1$-SubPcl$_3$-OPh 7** and ***C*$_3$-SubPcl$_3$-OPh 8** (dashed lines) in $CHCl_3$. d) Derivatives **1**–**4** in $CHCl_3$. e) Derivatives **1**–**4** and blend PBDB-T:***C*$_1$-OPh 1** y PBDB-T:***C*$_3$-OPh 2** in film.

Table 1. Optical and electrochemical parameters of the compounds under study.

C_X-R	Absorbance λ_{max} [nm]/log(ε) [a]	Absorbance in film λ_{max} [nm]	Emission λ_{max} [nm] [a]	E_g^{opt} [eV][b]	E_{red1} [eV][c]	LUMO [eV] [d]	HOMO [eV] [e]	μ_e [$cm^2\,V^{-1}\,s^{-1}$]
C_1-OPh 1	616/5.24	637	645	1.95	−1.01	−3.79	−5.74	1.9×10^{-5}
C_3-OPh 2	623/5.35	646	645	1.95	−1.06	−3.74	−5.69	1.7×10^{-5}
C_1-Cl 3	592/4.99	602	615	2.04	−1.43	−3.37	−5.41	–
C_3-Cl 4	624/5.21	642	641	1.96	−1.40	−3.40	−5.36	–

[a] Absorption and emission spectra were measured in $CHCl_3$. [b] E_g^{opt} was determined from the intersection of absorption and normalized emission spectra registered in $CHCl_3$ ($E_g^{opt} = 1240/\lambda$ [eV]). [c] Redox potentials were measured in CH_2Cl_2 with 0.1 M Bu_4NPF_6 vs. Fc/Fc^+, with graphite counter electrode and Ag/$AgNO_3$ as reference electrode. [d] LUMO was calculated by $LUMO = -|E_{red1}$ (vs. $Fc/Fc^+) + 4.8|$. [e] HOMO was calculated by HOMO=LUMO − E_g^{opt} (eV).

largest displacement (*i.e.* 54 nm) and C_1-**Cl 3** the smallest red-shift (*i.e.* 19 nm) (Figure 1b–1c). The bathochromic shift of the Soret and Q bands of the acceptors in comparison with the corresponding SubPc reference compounds is due to the increasing of the π-conjugation of the ring by the substitution of the peripheral positions of the SubPc core with three DPP units, Figure 1b–1c.[22] In films, the absorbance peaks of the four acceptors showed a broader shape due to the aggregation of the compounds in solid-state.

The absorption bands in films of C_1-**OPh 1**, C_3-**2**, C_1-**Cl 3** and C_3-**Cl 4** are centered at 637 nm, 646 nm, 602 nm and 642 nm, respectively, which result in a red-shift of 21 nm, 23 nm, 10 nm and 18 nm relative to the absorption peaks in solution. The bigger red-shift found for C_3-**OPh 2** may be associated with a stronger intermolecular aggregation in the solid state. The steady-state photoluminescence spectra of the four new acceptors were measured in $CHCl_3$ (Figure S16 and Table 1). As observed in absorption measurements, compound C_1-**Cl 3** had a broader emission spectrum, suggesting a higher tendency toward aggregation in solution than the other compounds. Stokes shift of all compounds vary between 17 and 29 nm, being C_3-**Cl 4** the compound with the lowest Stokes shift and C_1-**OPh 1** the one with the highest.

The HOMO and LUMO energy levels of the four acceptors were established by cyclic voltammetry (CV) and estimated using the onset values of reduction and oxidation potentials (Figure S17). To calculate LUMO levels, the following equation was used: $LUMO = -|E_{red1}$ (vs. $Fc/Fc^{+}) + 4.8|$. HOMO was calculated as HOMO=LUMO-E_g^{opt}. The derivatives with a OPh group in the axial position did not show great differences between them. For C_1-**OPh 1** and C_3-**OPh 2** LUMO values of −3.79 eV and −3.74 eV and HOMO values of −5.74 eV and −5.69 eV were estimated, respectively. Something similar was observed for derivatives with Cl in the axial position, with LUMO values of −3.37 eV and −3.40 eV for C_1-**Cl 3** and C_3-**Cl 4**, respectively. HOMO values of −5.41 eV and −5.36 eV were estimated for C_1-**Cl 3** and C_3-**Cl 4**, respectively, Figure 2a. Cl derivatives showed higher reduction potential values in the module compared to OPh derivatives values.

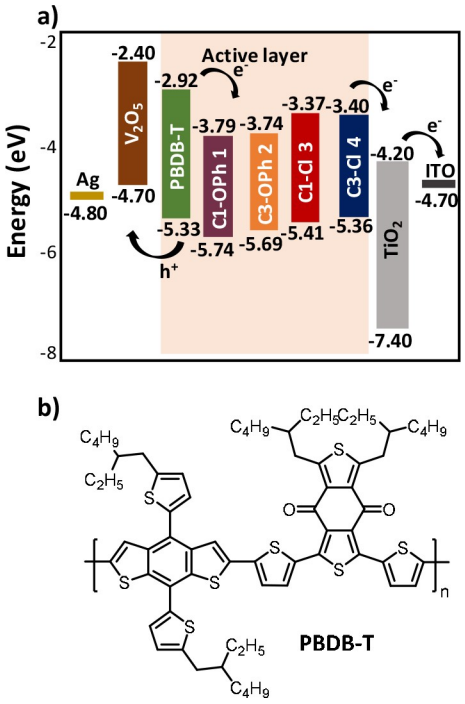

Figure 2. a) Energy levels diagram for the device layers. b) Donor polymer PBDB-T.

Photovoltaics

To evaluate the photovoltaic properties of the SubPc$(DPP)_3$-based acceptors, OSCs based on SubPc$(DPP)_3$ derivatives were fabricated using the inverted structure ITO/TiO_2/PBDB-T:SubPc$(DPP)_3$/V_2O_5/Ag. The energy levels of the different constituents used in the fabrication of solar devices are compiled in Figure 2a. The LUMO levels of the new acceptor materials are well aligned with the LUMO value of the donor polymer PBDB-T (Figure 2b). Nevertheless, it appears that the HOMO values of the derivatives with chlorine atoms in the axial position could accept holes from the environment, which could lead to a higher probability of recombination phenomena. The PBDB-T:SubPc$(DPP)_3$ devices were optimized in terms of annealing temperature, spin-casting speed, DIO additive concentration, and donor/acceptor (D/A) ratio. C_1-**OPh 1** and C_3-**OPh 2** showed higher solubility in chlorobenzene comparing to C_1-**Cl 3** and C_3-**Cl 4**. Among the four NFAs, C_1-**Cl 3** had the poorest solubility in chlorobenzene, so that PBDB-T: C_1-**Cl 3** was heated up to 80 °C till yielding a homogenous solution. The results of the OSCs optimization are summarized in Tables S1–S9 in the Supporting Information. The J_{SC} of OSCs increases when annealed up to 100 °C in comparison to devices without annealing. Nevertheless, by increasing the annealing temperature to 160 °C the J_{SC} of devices decreased. These results agree with the J_{SC} behaviour due to annealing temperature effect on inverted OSCs based on PBDB-T.[23] Li *et al.* reported that J_{SC} of PBDB-T:IT-M-based OSCs decreases because of a diffuse interface between PBDB-T and IT-M due to the large correlation length of PBDB-T when annealed at 160 °C.[24]

On the other hand, the performance of the devices increased as the concentration of DIO in chlorobenzene decreased from 2 to 0.5 %. However, the devices made without DIO additive showed the lowest performance with respect to the devices with DIO. Figure 3a shows the current density-voltage *(J-V)* curves of the best-performing optimized devices, whereas the best and average (parenthesis) values of performance characteristics are summarized in Table 2. The devices parameters were averaged over eight devices.

The devices made with OPh derivatives exhibited higher performance parameters than those constituted by SubPc$(DPP)_3$-Cl, having obtained the best performance with C_1-**OPh 1** devices and the worst with C_1-**Cl 3** which presented an efficiency of 3.17 % and 1.01 %, respectively.

In detail, for the SubPc$(DPP)_3$-OPh based OSCs similar performances were obtained for the two regioisomers C_1 and

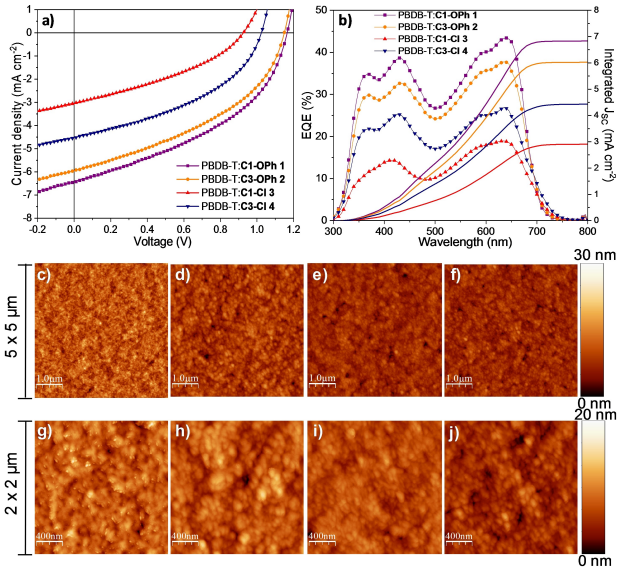

Figure 3. a) *J-V* curves and b) EQE spectra of the best-performing OSCs based on the optimized blends of PBDB-T blended with ***C1-OPh 1***, ***C3-OPh 2***, ***C*$_1$-Cl 3**, and ***C*$_3$-Cl 4** acceptors. AFM images for PBDB-T:***C*$_1$-OPh 1** (c, g), PBDB-T:***C*$_3$-OPh 2** (d, h), PBDB-T:***C*$_1$-Cl 3** (e, i), and PBDB-T:***C*$_3$-Cl 4** (f, j). The scan size is 5×5 µm (a–d) and 2×2 µm (e–h).

C_3. Nevertheless, the devices made with ***C*$_1$-OPh 1**, with a J_{SC} of 6.42 mA cm^{-2}, a V_{OC} of 1.17 V and a FF of 42.16%, proved to be slightly better than those based on ***C*$_3$-OPh 2** derivative (3.17% *vs* 2.83%, respectively). However, this similarity was not gained with Cl derivatives since with the C_3 regioisomer an efficiency twice greater than that obtained with C_1 was achieved. This result indicates that the symmetry of the peripheral substitution pattern influences the performance of OSCs when using a chloride atom in the axial position. For comparison, the BHJ-inverted polymer solar cells device based on PBDB-T:PC60BM (PC60BM from Solenne BV) was fabricated in the same conditions than SubPc(DPP)$_3$-based devices. The *J*-V characteristic under the illumination of PBDB-T:PC60BM and its performance parameters are shown in Figure S23. The devices based on the conventional PC60BM exhibited a V_{OC} of 0.80 V, a J_{SC} of 12.99 mA/cm^2, a FF of 48.70%, and a PCE of 5.09%. PC60BM-based devices shown a higher PCE (which is attributed to its higher J_{SC} value), and a slightly improved FF. As expected, the PC60BM-based device exhibited lower V_{OC} than that of SubPc(DPP)$_3$-based devices due to its lower LUMO value.

A pertinent result of the study of SubPc(DPP)$_3$-derivatives in OSCs was the high V_{oc} values than were achieved. Excluding ***C*$_1$-Cl 3**, all the other derivatives presented V_{oc} values higher than 1 V. These values stand out in relation to other published in the literature although the efficiencies obtained were not so high as intended.[25] The external quantum efficiency (EQE) spectra of the best-performing optimized devices are displayed in Figure 3b. All the OSCs exhibited broad EQE spectra from 300 to 800 nm as a result of the absorption of PBDB-T and the SubPc(DPP)$_3$ acceptors. In the range of 450–500 nm the EQE spectra suffered a slightly decrease since the SubPc(DPP)$_3$ acceptors have a limited absorption over this range (Figure 3b). The J_{SC} values determined by integrating of the EQE spectra were 6.83 mA cm^{-2} for PBDB-T:***C*$_1$-OPh 1**, 6.03 mA cm^{-2} for PBDB-T:***C*$_3$-OPh 2**, 2.91 mA cm^{-2} and 4.43 mA cm^{-2} for PBDB-T:***C*$_1$-Cl 3** and PBDB-T:***C*$_3$-Cl 4**, respectively, agreeing with the J_{SC} calculated from the *J*-V characteristics (refers Table 2).

Since the morphology of the active layer plays an important role in the exciton dissociation and charge carrier transport performance of OSCs, the morphologies of the PBDB-T:SubPc(DPP)$_3$ films were analyzed by atomic force spectroscopy (AFM). Thin films of active layers were deposited on TiO_2-covered ITO substrates in identical conditions to those of solar cell devices. Figure 3c–3j show the AFM images for the active layers from the different SubPc(DPP)$_3$ acceptors. As shown, all the blend thin films had a similarly smooth surface. The root-mean-square roughness (RMS) values, as well as the peak-to-peak height for the PBDB-T:SubPc thin films, are summarized in Table S10. The thin films showed an RMS in the range of 1.45–2.09 nm. However, thin films made with ***C*$_1$-Cl 3** and ***C*$_3$-Cl 4** exhibited less roughness (1.45 nm and 1.54 nm, respectively) than thin films made with OPh derivatives (**1.98 nm** and **2.09 nm** for ***C*$_1$-OPh 1** and ***C*$_3$-OPh 2,** respectively). In addition, thin films made with OPh derivatives presented higher peak-to peak values (17.57 nm and 15.34 nm for ***C*$_1$-OPh 1** and ***C*$_3$-OPh 2**, respectively) than that of thin films made with ***C*$_1$-Cl 3** and ***C*$_3$-Cl 4** (12.21 nm and 12.11 nm, respectively). Complementarily, the AFM 3D-images (Figure S18) revealed that all the PBDB-T:SubPc(DPP)$_3$ thin films have the similar "mountain and valley"-like aspect and no significant differences were found in the morphology of all thin films. Therefore, we assume that the reason for the limited efficiency of devices made with ***C*$_1$-Cl 3** and ***C*$_3$-Cl 4** could lie on the degree of recombination dynamics and exciton dissociation.[26] Among the different SubPc(DPP)$_3$-derivatives, those with OPh-substituted species (i.e. ***C*$_1$-OPh 1** and ***C*$_3$-OPh 2**) demonstrated to be more promising acceptors for OSCs applications. To further investigate the electrical properties of the ***C*$_1$-OPh 1** and ***C*$_3$-OPh 2**, we carried out electron mobility measurements on electron-only devices with

Table 2. Performance parameters of optimized OSCs based on PBDB-T blended with SubPc(DPP)$_3$-derivative acceptors.

Active Layer	V_{OC} [V][a]	J_{SC} [mA cm^{-2}] [a]	J_{SC} [EQE] [mA cm^{-2}]	FF [%][a]	PCE [%][a]	R_S [Ω cm^2][a]	R_{Sh} [Ω cm^2][a]
PBDB-T:C_1-OPh 1	1.17 (1.16)	6.42 (6.39)	6.83	42.16(41.63)	3.17 (3.08)	24.03 (24.80)	449.09 (439.76)
PBDB-T:C_3-OPh 2	1.15 (1.14)	5.95 (5.91)	6.03	41.35 (38.98)	2.83 (2.62)	22.79 (26.34)	477.56 (417.48)
PBDB-T:C_1-Cl 3	0.93 (0.89)	3.04 (2.89)	2.91	35.72 (36.07)	1.01 (0.91)	33.37 (27.50)	561.76 (621.95)
PBDB-T:C_3-Cl 4	1.02 (0.99)	4.50 (4.23)	4.43	42.02 (39.58)	1.93 (1.68)	10.62 (12.54)	580.19 (547.45)

[a] Maximum value and average (in brackets) over eight devices.

the structure ITO/ZnO/***C*$_1$-OPh 1** or ***C*$_3$-OPh 2**/Al. The *J*-V curves of electron-only devices are depicted in Figure S20. From the graph, we identified three characteristic space-charge-limited current (SCLC) regions:[27] i) the Ohmic region at low voltages, with slope SI = 1, ii) the trap-filled limited (TFL) region at medium voltages, with slope SII = 2 and SII > 2 when the current is limited by shadow and deep traps, respectively, and iii) the trap-free region at high voltages, with slope SIII = 2. In this last region, the trap-free electron mobility can be calculated using Mott-Gurney's law:

$$J_{SCLC} = \frac{9}{8}\,\mu\,\varepsilon_0\varepsilon_r\frac{V^2}{L^3} \quad (1)$$

where μ is the charge carrier mobility, ε_0 is the permittivity of vacuum, ε_r is the relative permittivity of the SubPc derivatives, V is the voltage and L is the sample thickness. The calculated electron mobilities of the ***C*$_1$-OPh 1** and ***C*$_3$-OPh 2** acceptors were 1.9×10^{-5} cm^2 V^{-1}s^{-1} and 1.7×10^{-5} cm^2 V^{-1}s^{-1}, respectively. Although the electron mobility of both acceptors is similar, Figure S24 shows higher current density values for ***C*$_1$-OPh 1** devices at a voltage given which is in good agreement with their higher efficiency when used as active layer in solar cells. These results can be correlated with the electron trap-state density value, Nt, calculated using.[28]

$$V_{TFL} = \frac{eN_t\,L^2}{2\varepsilon_0\varepsilon_r} \quad (2)$$

where V_{TFL} is the trap-filled limit voltage, e is the elementary charge, L is the thickness of ***C*$_1$-OPh 1** and ***C*$_3$-OPh 2** films, ε_0 is the vacuum permittivity, and ε_r is the relative dielectric constant of ***C*$_1$-OPh 1** and ***C*$_3$-OPh 2**. The calculated N_t of ***C*$_1$-OPh 1** was 4.5×10^{17} cm^{-3}, while the N_t of ***C*$_3$-OPh 2** is slightly higher (5.7×10^{17} cm^{-3}). The combination of higher electron mobility and lower electron trap density of ***C*$_1$-OPh 1** could explain the enhanced performance of devices based on PBDB-T:***C*$_1$-OPh 1** in comparison to the those based on PBDB-T:***C*$_3$-OPh 2**.

Conclusion

The synthesis and characterization of four new star-shaped electron acceptors based on a SubPc core decorated with three DPP wings linked through an acetylene bridge are reported. The four compounds present a broad absorption in the 450–700 nm range. Unexpectedly, the absorption spectrum of ***C*$_1$-Cl 3** was found to slightly differ from that of the other derivatives, as it exhibits a broader Q-band with a lower molar extinction coefficient. All these materials were probed as acceptors in BHJ-inverted polymer solar cells, with the polymer PBDB-T as the donor counterpart. ***C*$_1$-OPh 1** produced the highest parameters, with a V_{oc} as high as 1.17 V, a PCE of 3.17%, a J_{sc} of 6.42 mA/cm^2 and a FF of 42.16%. These results can be attributed to the good electron mobility and low electron trap density of the ***C*$_1$-OPh 1** acceptor. Unlike, ***C*$_1$-Cl 3** gave rise to the lowest photovoltaic parameters, resulting in a discreet PCE of 1.01%. Although ***C*$_3$-Cl 4** reached a FF higher than ***C*$_3$-OPh 2** (42.16% *vs.* 41.35%), the latter afforded better PCE due to the higher V_{oc} and J_{sc} values. In summary, the conjugates featuring the OPh group in the axial position gave the best results as acceptors in the studied conditions. Whereas for the axially chlorinated derivatives it was found that the C_1 regioisomer present better photovoltaic parameters than the C_3 species, for the OPh-substituted species the two regioisomers afforded similar values. Despite the relatively low J_{SC} of OSCs based on our SubPc(DPP)$_3$-derivative acceptors, these devices exhibited exceptionally high V_{OC} (> 1 V). For this reason, they are high promising NFAs for application in ternary OSCs in which a high V_{OC} is desired.

Experimental Section

Measurement and characterization

^{1}H NMR data were recorded at 25 °C with a Bruker AC300 and A400 spectrometer with chemical shifts referenced to residual TMS. Matrix-assisted laser desorption/ionization time-of-flight (MALDI-TOF) mass spectra were obtained on a Bruker Microflex LRF20 instrument using dithranol as a matrix. Cyclic voltammetry measurements were performed in 0.1 M tetrabutylammonium hexafluorophosphate dichloromethane solution as support electrolyte, a graphite working electrode, an Ag/Ag$^+$ reference electrode, and carbon counter electrode using a potentiostat/galvanostat μAutolab Type III. Ferrocene/ferrocenium redox couple (Fc/Fc$^+$) was used as an internal standard for all measurements, and 4.8 eV under vacuum was established as the reference level. UV-vis spectra in $CHCl_3$ solution were measured with a Helios Gamma spectrophotometer and the extinction coefficients were calculated using the Lambert-Beer Law. Emission measurements were recorded in Perkin Elmer LS 55 fluorometer. IR spectra were measured with a Nicolet Impact 400D spectrophotometer.

Materials

All chemicals and solvents were purchased from Sigma Aldrich (Merck) and TCI and were used without further purification unless otherwise stated. **DPP 9** was synthesized according to the literature.[29] Column chromatography was performed with SiO_2 (40–63 μm), and preparative TLC plate was used with 1 mm of silica gel 60 with indicator UV_{254}.

Synthesis

Synthesis of SubPc-(DPP)$_3$ derivatives. To a 25 mL round-bottom flask, the corresponding triiodide subphthalocyanine (50 mg, 0.055 mmol), tris(dibenzylideneacetone)dipalladium(0), $Pd_2(dba)_3$ (31 mg, 0.035 mmol), CuI (6.8 mg, 0.035 mmol), PPh_3 (75 mg, 0.288 mmol) and 1 mL of anhydrous toluene were added under nitrogen. Then, 2 mL of triethylamine were added, and the solution was deoxygenated. Finally, a degassed solution containing DPP 9 (100 mg, 0.18 mmol) in 4 mL of toluene was added. After that, the crude was washed with 2 M HCl and water and extracted with chloroform. The compounds were obtained in the form of dark blue solids.

***C*$_1$-OPh 1**. The compound was purified by silica gel column chromatography using different ratio of $CHCl_3$/ ethyl acetate as eluent. Yield: 17%. ^{1}H NMR (300 MHz, $CDCl_3$): δ (ppm) 9.04–9.02 (m,

3H), 8.96–8.93 (m, 6H), overlapping doublets centered at 8.03 and 8.02 (d, 3H, J_1 = 9 Hz), 8.04 (d, 3H, J_1 = 6.0 Hz), 7.65 (d, 3H, J_1 = 6.0 Hz), 7.51 (d, 3H, J_1 = 3.0 Hz), 7.30–7.27 (m, 3H), 6.80 (d, 2H, J_1 = 9.0 Hz), 5.35 (d, 2H, J_1 = 9.0 Hz), 4.12–3.99 (m, 12H), 1.94–1.89 (m, 6H), 1.45-1.25 (m, 48H), 1.10 (s, 9H), 0.96–0.85 (m, 36H). FT-IR (KBr) ν: 2960, 2924, 2856, 2187, 1665, 1640, 1553, 1509, 1456, 1400, 1324, 1289, 1257, 1230, 1175, 1091, 1060, 1020, 856, 826, 761, 734, 707 cm^{-1}. UV/Vis ($CHCl_3$), λ_{max} (log ε):303 (4.91), 372 (4.80), 616 (5.24). MALDI-TOF (MS, dithranol): m/z = 2184.2 $[M+H]^+$.

C_3-OPh 2. The compound was purified by silica gel column chromatography using different ratio of $CHCl_3$/ ethyl acetate as eluent. Yield: 73%. ^{1}H NMR (300 MHz, $CDCl_3$): δ (ppm) 9.031–9.028 (m, 3H), 8.96–8.93 (m, 6H), 8.81 (dd, 3H, J_1 = 8.82 Hz, J_2 = 0.3 Hz), 8.03 (dd, 3H, J_1 = 8.4 Hz, J_2 = 1.2 Hz), 7.65 (dd, 3H, J_1 = 5.0 Hz, J_2 = 1.1 Hz), 7.50 (d, 3H, J_1 = 6.0 Hz), 7.29–7.28 (m, 3H), 6.80 (d, 2H, J_1 = 6.0 Hz), 5.35 (d, 2H, J_1 = 6.0 Hz), 4.12–3.99 (m, 12H), 1.94–1.89 (m, 6H), 1.48–1.26 (m, 48H), 1.10 (s, 9H), 0.96–0.85 (m, 36H). FT-IR (KBr) ν: 2925, 1666, 1554, 1453, 1399, 1230, 1175, 1062, 827, 761, 134, 706 cm^{-1}. UV/Vis ($CHCl_3$), λ_{max} (log ε):302 (5.00), 369 (4.90), 553 (5.15), 623 (5.41). MALDI-TOF (MS, dithranol): m/z = 2184.2 $[M+H]^+$.

C_1-Cl 3. The compound was purified by preparative TLC plate using 2:1 $CHCl_3$/ ethyl acetate as eluent. Yield: 15%. ^{1}H NMR (400 MHz, $CDCl_3$): δ (ppm) 9.08–9.07 (m, 3H), 8.96 (d, 3H, J_1 = 8 Hz), 8.94 (d, 3H, J_1 = 4 Hz), overlapping doublets centered at 8.87 and 8.86 (d.3H, J_1 = 8 Hz), 8.09 (d, 3H, J_1 = 8 Hz), 7.66 (d, 3H, J_1 = 4 Hz), 7.52 (d, 3H, J_1 = 8 Hz), 7.29 (t, 3H, J_1 = 4 Hz), 4.11–4.00 (m, 12H), 1.94–1.89 (m, 6H), 1.45–1.25 (m, 57H), 0.96–0.85 (m, 38H). FT-IR (KBr) ν: 2956, 2927, 2858, 2188, 1730, 1666, 1613, 1555, 1509, 1455, 1401, 1327, 1292, 1264, 1231, 1179, 1096, 1021, 977, 890, 858, 827, 789, 766, 735, 709 cm^{-1}. UV/Vis (toluene), λ_{max} (log ε):373 (4.65), 595 (4.90). MALDI-TOF (MS, dithranol): m/z = 2068.9 $[M]^+$.

C_3-Cl 4. The compound was purified by preparative TLC plate using 100% CH_2Cl_2 as eluent. Yield: 8%. ^{1}H NMR (400 MHz, $CDCl_3$): δ (ppm) 9.05–9.04 (m, 3H), 8.97–8.94 (m, 6H), 8.82 (dd, 3H, J_1 = 8.1 Hz, J_2 = 0.9 Hz), 8.05 (dd, 3H, J_1 = 8.0 Hz, J_2 = 1.6 Hz), 7.66 (dd, 3H, J_1 = 6.8 Hz, J_2 = 1.6 Hz), 7.51 (d, 3H, J_1 = 8 Hz), 7.31–7.28 (m, 3H), 4.08–4.05 (m, 12H), 1.94–1.85 (m, 6H), 1.45–1.25 (m, 60H), 0.96–0.85 (m, 36H). FT-IR (KBr) ν: 2954, 2954, 2856, 2189, 1731, 1666, 1613, 1554, 1509, 1453, 1400, 1381, 1305, 1264, 1230, 1178, 1095, 1065, 1021, 977, 891, 857, 827, 790, 734, 707, 663 cm^{-1}. UV/Vis (toluene), λ_{max} (log ε): 373 (4.73), 628 (5.19). MALDI-TOF (MS, dithranol): m/z = 2068.9 $[M]^+$.

Synthesis of 4-*tert*-butylphenoxy-SubPc derivatives (C_1-SubPcl$_3$-OPh 5 and C_3-SubPcl$_3$-OPh 6). SubPcl$_3$-OPh was synthetized as a mixture of C_1 and C_3 regioisomers by substitution of the axial halide atom in **SubPcl$_3$-Cl** in a one-pot process, which was performed by treatment of the crude cyclotrimerization product with 4-*tert*-butylphenol in toluene at reflux for 16 h.[30] The purification of **SubPcl$_3$-OPh** was carried out by column chromatography on silica gel using toluene as solvent, which allowed to isolate the C_3 and C_1 regioisomers.

Synthesis of chloro-SubPc derivatives (C_1-SubPcl$_3$-Cl 7 and C_3-SubPcl$_3$-Cl 8): Chloro SubPcs **7** and **8** were obtained in the expected 3:1 statistical ratio by condensation of 4-iodophthalonitrile in the presence of boron trichloride in refluxing *p*-xylene according to a procedure previously reported by us.[31] The constitutional isomers were separated by column chromatography on silica gel employing toluene as eluent, as a variation of the conditions described in the literature.[32]

OSC devices fabrication and characterization: The best performing of OSCs-based on **C_1-OPh 1**, **C_3-OPh 2**, and **C_3-Cl 4** was obtained under the optimized conditions with the weight ratio of PBDB-T:NFAs = 1:1, dissolved in chlorobenzene: DIO ratio of 99.5:0.5 v/v with a final concentration of 20 mg mL^{-1}. For OSCs based on PBDB-T:**C_1-Cl 3** the optimized weight ratio of was 1:1 dissolved in chlorobenzene: DIO ratio of 99:1 v/v with a final concentration of 20 mg mL^{-1}. All the PBDB-T:NFA solutions were deposited on top of TiO_2 film at 5000 rpm by 45 s, then PBDB-T:NFA films were thermally annealed at 100 °C by 10 min. The detailed devices fabrication is described in the Supporting Information. The *J*-V curves of the OSCs devices were recorded using a Keithley 2400 source-measure unit under 100 mW cm^2 AM 1.5G light illumination provided by a solar simulator (Abet Technologies model 11 000 class type A, Xenon arc). The EQE measurements were taken under forward wavelength sweep direction from 300 nm to 800 nm using Lasing IPCE-DC system with a serial number of LS1109-232.The AFM images of the samples were recorded in tapping mode on a Molecular Imaging model Pico SPM II (pico +). Images were collected in the air using silicon probes with a typical spring constant of 1–5 nN/m, and at a resonant frequency of 75 kHz.

Acknowledgements

ASS and TT thank to the Spanish Ministerio de Ciencia e Innovación (MICINN/FEDER) by financial support (CTQ2017-87102-R and CTQ2017-85393-P). Financial support from MINECO, Spain (PCI2019-111889-2) and ERA-NET/European Commission (UNIQUE, SOLAR-ERA.NET Cofound 2 N° 008), is also acknowledged (TT). MJAM thanks to "Beca Santiago Grisolia Grisoliap20177153" de la Comunidad Valenciana. JGS, JP and LFM thank to the Spanish Ministerio de Ciencia e Innovación (MICINN/FEDER) RTI2018-094040-B–I00, the Agency for Management of University and Research Grants (AGAUR) ref 2017-SGR-1527, and the Catalan Institution for Research and Advanced Studies (ICREA) under the ICREA Academia Award. IMDEA Nanociencia acknowledges support from the "Severo Ochoa" Programme for Centres of Excellence in R&D (MINECO, Grant SEV2016-0686).

Conflict of Interest

There are no conflicts to declare.

Keywords: diketopyrrolopyrroles · non-fullerene acceptor · organic solar cells · π-systems · subphthalocyanines

[1] a) A. M. Bagher, *Sustain. Energy.* **2014**, *2*, 85; b) G. Li, R. Zhu, Y. Yang, *Nat. Photonics* **2012**, *6*, 153–161; c) Y. Sun, M. Chang, L. Meng, X. Wan, H. Gao, Y. Zhang, K. Zhao, Z. Sun, C. Li, S. Liu, H. Wang, J. Liang, Y. Chen, *Nat. Electron.* **2019**, *2*, 513–520.
[2] B. Ecker, J. C. Nolasco, J. Pallarés, L. F. Marsal, J. Posdorfer, J. Parisi, E. von Hauff, *Adv. Funct. Mater.* **2011**, *21*, 2705.
[3] K.-L. Ou, D. Tadytin, K. X. Steirer, D. Placencia, M. Nguyen, P. Lee, N. R. Armstrong, *J. Mater. Chem. A* **2013**, *1*, 6794–6803.
[4] J. G. Sánchez, V. S. Balderrama, S. I. Garduño, E. Osorio, A. Viterisi, M. Estrada, J. Ferré-Borrull, J. Pallarès, L. F. Marsal, *RSC Adv.* **2018**, *8*, 13094–13102.
[5] a) V. S. Balderrama, J. G. Sánchez, G. Lastra, W. Cambarau, S. Arias, J. Pallarès, E. Palomares, M. Estrada, L. F. Marsal, *J. Mater. Chem. A* **2018**, *6*, 22534–22544; b) Z. He, C. Zhong, S. Su, M. Xu, H. Wu, Y. Cao, *Nat. Photonics* **2012**, *6*, 593–595.
[6] a) R. C. I. MacKenzie, V. S. Balderrama, S. Schmeisser, R. Stoof, S. Greedy, J. Pallarès, L. F. Marsal, A. Chanaewa, E. von Hauff, *Adv. Energy Mater.*

2016, *6*, 1501742; b) G. Terán-Escobar, J. Pampel, J. M. Caicedo, M. Lira-Cantú, *Energy Environ. Sci.* **2013**, *6*, 3088–3098.
[7] X. Li, F. Xie, S. Zhang, J. Hou, W. C. Choy, *Light-Sci. Appl.* **2015**, *4*, e273.
[8] I. Etxebarria, J. Ajuria, R. Pacios, *J. Photonics Energy* **2015**, *5*, 057214–1–25.
[9] P. Cheng, G. Li, X. Zhan, Y. Yang, *Nat. Photonics* **2018**, *12*, 131–142.
[10] a) J. Zhang, H. S. Tan, X. Guo, A. Facchetti, H. Yan, *Nat. Energy* **2018**, *3*, 720–731; b) Y. Sun, H.-H. Gao, Y.-Q.-Q. Yi, X. Wan, H. Feng, X. Ke, Y. Zhang, J. Yan, C. Li, Y. Chen, *Sci. China Mater.* **2019**, *62*, 1210–1217.
[11] a) Y.-Q. Pan, G.-Y. Sun, *ChemSusChem* **2019**, *12*, 4570–4600; b) X. Huang, M. Hu, X. Zhao, C. Li, Z. Yuan, X. Liu, C. Cai, Y. Zhang, Y. Hu, Y. Chen, *Org. Lett.* **2019**, *21*, 3382–3386; c) H. Hang, X. Wu, Q. Xu, Y. Chen, H. Li, W. Wang, H. Tong, L. Wang, *Dyes Pigm.* **2019**, *160*, 243–251; d) Y. N. Luponosov, A. N. Solodukhin, A. L. Mannanov, P. S. Savchenko, Y. Minenkov, D. Y. Paraschuk, S. A. Ponomarenko, *Dyes Pigm.* **2020**, *177*, 108260; e) K. Wang, P. Xia, K. Wang, Xi. You, M. Wu, H. Huang, D. Wu, J. Xia, *ACS Appl. Mater. Interfaces* **2020**, *12*, 9528–9536; f) A. Stanculescua, C. Breazua, M. Socol, O. Rasoga, N. Preda, G. Petre, A. M. Solonaru, M. Grigoras, F. Stanculescu, G. Socol, G. Popescu-Pelin, M. Girtan, *Appl. Surf. Sci.* **2020**, *509*, 145351; g) J. Hu, X. Liu, K. Wang, M. Wu, H. Huang, D. Wu, J. Xia, *J. Mater. Chem. C* **2020**, *8*, 2135–2141.
[12] a) B. A. Gregg, *J. Phys. Chem. Lett.* **2011**, *2*, 3013; b) C. Zhan, X. Zhang, J. Yao, *RSC Adv.* **2015**, *5*, 93002; c) Q. Zhang, X. Xu, S. Chen, G. B. Bodedla, M. Sun, Q. Hu, Q. Peng, B. Huang, H. Ke, F. Liu, T. P. Russell, X. Zhu, *Sustain. Energy Fuels* **2018**, *2*, 2616–2624; d) C. Jiang, X. Huang, B. Sun, Y. Li, M. Gao, L. Ye, H. Ade, S. R. Forrest, J. Fan, *Org. Lett.* **2020**, *84*, 105784.
[13] A. Wadsworth, M. Moser, A. Marks, M. S. Little, N. Gasparini, C. J. Brabec, D. Baran, I. McCulloch, *Chem. Soc. Rev.* **2019**, *48*, 1596–1625.
[14] a) T. M. Grant, D. S. Josey, K. L. Sampson, T. Mudigonda, T. P. Bender, B. H. Lessard, *Chem. Rec.* **2019**, *19*, 1093–1112; b) G. de la Torre, G. Bottari, T. Torres, *Adv. Energy Mater.* **2017**, *7*, 1601700; c) C. G. Claessens, D. Gonzalez-Rodriguez, M. S. Rodriguez-Morgade, A. Medina, T. Torres, *Chem. Rev.* **2014**, *114*, 2192–2277; d) G. E. Morse, T. P. Bender, *ACS Appl. Mater. Interfaces* **2012**, *4*, 5055–2068; e) A. Medina, C. G. Claessens, *J. Porphyrins Phthalocyanines* **2009**, *13*, 446–454.
[15] a) Y.-Q. Zheng, J.-L. Yu, W.-G. Li, J. Tang, B. Wei, X.-F. Li, J.-F. Shi, J.-H. Zhang, Y.-F. Wang, *J. Phys. D* **2020**, *53*, 125102; b) M. Xiao, Y. Tian, S. Zheng, *Org. Electron.* **2018**, *59*, 279–287; c) E. Jouad, E. M. El-Menyawy, G. Louarn, L. Arzel, M. Morsli, M. Addou, J. C. Bernède, L. Cattin, *J. Phys. Chem. Solids* **2020**, *136*, 109142; d) C. C. Lee, W. C. Su, Y. S. Shu, W. C. Chang, B. Y. Huang, Y. Z. Lee, T. H. Su, K. T. Chen, S. W. Liu, *RSC Adv.* **2015**, *5*, 5617–5626; e) N. Wang, X. Tong, Q. Burlingame, J. Yu, S. R. Forrest, *Sol. Energy Mater. Sol. Cells* **2014**, *125*, 170–175.
[16] a) B. Ebenhoch, N. B. A. Prasetya, V. M. Rotello, G. Cooke, I. D. W. Samuel, *J. Mater. Chem. A* **2015**, *3*, 7345–7352; b) T. M. Grant, D. S. Josey, K. L. Sampson, T. Mudigonda, T. P. Bender, B. H. Lessard, *Chem. Rec.* **2019**, *19*, 1093–1112.
[17] K. Cnops, B. P. Rand, D. Cheyns, B. Verreet, M. A. Empl, P. Heremans, *Nat. Commun.* **2014**, *5*, 3406.
[18] X. Huang, M. Hu, X. Zhao, C. Li, Z. Yuan, X. Liu, C. Cai, Y. Zhang, Y. Hu, Y. Chen, *Org. Lett.* **2019**, *21*, 9, 3382–3386.
[19] a) Y. Patil, R. Misra, *J. Mater. Chem. C* **2019**, *7*, 13020; b) S. Loser, S. J. Lou, B. M. Savoie, C. J. Bruns, A. Timalsina, M. J. Leonardi, J. N. Smith, T. Harschneck, R. Turrisi, N. Zhou, C. L. Stern, A. A. Sarjeant, A. Facchetti, R. P. H. Chang, S. I. Stupp, M. A. Ratner, L. X. Chen, T. J. Marks, *J. Mater. Chem. A* **2017**, *5*, 13020–13031; c) M. Grzybowski, D. T. Gryko, *Adv. Opt. Mater.* **2015**, *3*, 280–320.
[20] a) H.-H. Gao, Y. Sun, S. Li, X. Ke, Y. Cai, X. Wan, H. Zhang, C. Li, Y. Chen, *Dyes Pigm.* **2020**, *176*, 108250; b) M. Grzybowski, D. T. Gryko, *Adv. Opt. Mater.* **2015**, *3*, 280–320; c) Q. Liu, S. E. Bottle, P. Sonar, *Adv. Mater.* **2020**, *32*, 1903882; d) K. Gao, S. B. Jo, X. Shi, L. Nian, M. Zhang, Y. Kan, F. Lin, B. Kan, B. Xu, Q. Rong, L. Shui, F. Liu, X. Peng, G. Zhou, Y. Cao, A. K.-Y. Jen, *Adv. Mater.* **2019**, *31*, 1807842.
[21] C. Yu, Z. Liu, Y. Yang, J. Yao, Z. Cai, H. Luo, G. Zhang, D. Zhang, *J. Mater. Chem. C* **2014**, *2*, 10101–10109.
[22] C. G. Claessens, D. G. -Rodríguez, M. S. R. -Morgade, A. M. T. Torres, *Chem. Rev.* **2014**, *114*, 2192–2277.
[23] J. G. Sanchez, A. A. A. Torimtubun, V. S. Balderrama, M. Estrada, J. Pallares, L. F. Marsal, *IEEE J. Electron Devices Soc.* **2019**, *8*, 421–428.
[24] W. Li, J. Cai, Y. Yan, F. Cai, S. Li, R. S. Gurney, D. Liu, J. D. McGettrick, T. M. Watson, Z. Li, A. J. Pearson, D. G. Lidzey, J. Hou, T. Wang, *Solar RRL* **2018**, *2*, 1800114.
[25] a) Y. Cui, H. Yao, J. Zhang, K. Xian, T. Zhang, L. Hong, Y. Wang, Y. Xu, K. Ma, C. An, C. He, Z. Wei, F. Gao, J. Hou, *Adv. Mater.* **2020**, *32*, 1908205; b) Y. Lin, Y. Firdaus, F. H. Isikgor, M. I. Nugraha, E. Yengel, G. T. Harrison, R. Hallani, A. E. -Labban, H. Faber, C. Ma, X. Zheng, A. Subbiah, C. T. Howells, O. M. Bakr, I. McCulloch, S. D. Wolf, L. Tsetseris, T. D. Anthopoulos, *ACS Energy Lett.* **2020**, *5*, 2935–2944.
[26] H. Cha, S. Wheeler, S. Holliday, S. D. Dimitrov, A. Wadsworth, H. H. Lee, D. Baran, I. McCulloch, J. R. Durran, *Adv. Funct. Mater.* **2018**, *28*, 1704389.
[27] a) H. F. Haneef, A. M. Zeidell, O. D. Jurchescu, *J. Mater. Chem. C* **2020**, *3*, 759–787; b) F. C. Chiu, *Adv. Mater. Sci. Eng.* **2014**, *2014*, 1–18.
[28] a) B. Wang, Y. Fu, C. Yan, R. Zhang, Q. Yang, Y. Han, Z. Xie, *Front. Chem.* **2018**, *6*, 1; b) X. Meng, C. H. Y. Ho, S. Xiao, Y. Bai, T. Zhang, C. Hu, H. Lin, Y. Yang, S. K. So, S. Yang, *Nano Energy* **2018**, *52*, 300–306.
[29] C. Yu, Z. Liu, Y. Yang, J. Yao, Z. Cai, H. Luo, G. Zhang, D. Zhang, *J. Mater. Chem. C* **2014**, *2*, 10101–10109.
[30] a) C. G. Claessens, M. J. Vicente-Arana, T. Torres, *Chem. Commun.* **2008**, 6378–6380; b) I. Sanchez-Molina, B. Grimm, R. M. Krick Calderon, C. G. Claessens, D. M. Guldi, T. Torres, *J. Am. Chem. Soc.* **2013**, *135*, 10503–10511.
[31] C. G. Claessens, D. González-Rodríguez, B. del Rey, T. Torres, G. Mark, H.-P. Schuchmann, C. von Sonntag, J. G. MacDonald, R. S. Nohr, *Eur. J. Org. Chem.* **2003**, 2547–2551.
[32] C. G. Claessens, T. Torres, *Tetrahedron Lett.* **2000**, *41*, 6361–6365.

Manuscript received: March 1, 2021
Revised manuscript received: April 28, 2021

FULL PAPERS

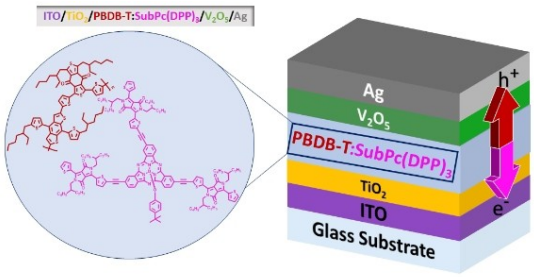

M. J. Álvaro-Martins, Dr. J. G. Sánchez, G. Lavarda, Dr. D. Molina, Dr. J. Pallarès, Prof. T. Torres, Prof. L. F. Marsal*, Prof. Á. Sastre-Santos**

Four electron acceptors comprising a subphthalocyanine core bearing three diketopyrrolopyrrole wings linked by an acetylene bridge have been synthesized. These derivatives feature *tert*-butylphenoxy and chlorine as axial substituents and for each of them, both the C_1 and the C_3 regioisomers have been prepared. These materials were applied in the active layer of inverted bulk-heterojunction polymer solar cells in combination with the donor polymer PBDB-T. C_1-SubPc-DPP-OPh (see figure) showed the best performances with a PCE of 3.27 %.